

# Assessing climate impact on forest cover in areas undergoing substantial land cover change using Landsat imagery

Qinli Yang<sup>a,b</sup>, Heng Zhang<sup>a</sup>, Wanshan Peng<sup>a</sup>, Yaoyao Lan<sup>a</sup>, Shasha Luo<sup>a</sup>, Junming Shao<sup>c</sup>, Dongzi Chen<sup>a</sup>, Guoqing Wang<sup>b,\*</sup>

<sup>a</sup> School of Resources and Environment, University of Electronic Science and Technology of China, Chengdu, China, No. 2006 Xiyuan Ave, West Hi-Tech Zone, Chengdu 611731, PR China

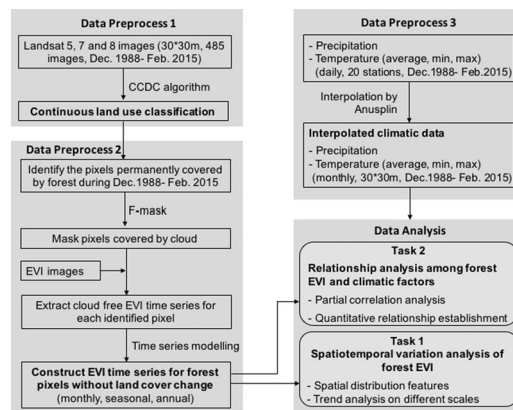
<sup>b</sup> State Key Laboratory of Hydrology-Water Resources and Hydraulic Engineering, Nanjing Hydraulic Research Institute, Nanjing, China, No. 225 Guangzhou Road, Nanjing 210029, PR China

<sup>c</sup> School of Computer Science and Engineering, University of Electronic Science and Technology of China, Chengdu, China, No. 2006 Xiyuan Ave, West Hi-Tech Zone, Chengdu 611731, PR China

## HIGHLIGHTS

- The framework allows for assessing climate impact on forest cover more precisely.
- Human-induced land cover change was excluded from assessing climate impact on forest cover.
- Climate-induced spatiotemporal variations of forest EVI on different scales were analyzed.
- Minimum temperature and precipitation are two key control factors for forest EVI.
- Quantitative relationship among forest EVI and climatic factors is established.

## GRAPHICAL ABSTRACT



## ARTICLE INFO

### Article history:

Received 29 August 2018

Received in revised form 12 November 2018

Accepted 19 December 2018

Available online 28 December 2018

Editor: Ralf Ludwig

### Keywords:

Enhanced vegetation index (EVI)

Spatiotemporal variation analysis

Partial correlation analysis

Remote sensing

## ABSTRACT

In this study, we propose to assess climate impact on forest cover (represented by EVI) at multiple scales in areas undergoing substantial land cover change, using Landsat imagery with human-induced land cover change effect excluded. Taking the Qingliu River catchment located in a subtropical humid monsoon area in China as a case study, the results indicate that EVI increases significantly ( $p < 0.01$ ) during 1989–2014 with a magnitude of 0.026/decade. Spatial distribution of EVI is distinct in summer and growing season. Temperature and precipitation show high partial correlations with EVI, with better partial correlation found between EVI and temperature. Their partial correlations with EVI on monthly scale are higher than those on annual scale. Besides, precipitation and pan evaporation show accumulative lag effects (4 months) on forest EVI, while temperature has no lag effect. Finally, an empirical formula is established to quantify the relationship among EVI and its main driving factors (temperature and precipitation) by considering the precipitation threshold (200 mm). The findings should provide scientific supports for local forest management and ecosystem services, and should also support the hydrological effect assessment of vegetation cover change under climate change for the study area.

© 2019 Elsevier B.V. All rights reserved.

\* Corresponding author.

E-mail address: [gqwang@nhri.cn](mailto:gqwang@nhri.cn) (G. Wang).

1. Introduction

1.1. Remote sensing of vegetation cover change

Climate is the most primary control factor for vegetation distribution (Sykes, 2009; Gao et al., 2016). Investigating the impact of climate change on vegetation cover dynamics is of great importance for global and regional ecosystem assessment and management (Walther et al., 2002; Sun et al., 2015; Jiang et al., 2017). Numerous studies concerning the effect of climate change on vegetation cover have shown that due to the spatiotemporal variations in climate change and eco-environmental conditions, the change patterns of vegetation cover are different among different regions (Hou et al., 2015). For instance, Wang et al. (2011) found that the spring vegetation greening trends were reversed between northwest and northeast in North America. Climatic factors (e.g., temperature, precipitation, relative humidity, photosynthetically active radiation (PAR)) especially for temperature and precipitation have been found to be significant driving factors for vegetation cover change (Zhou et al., 2015; Wen et al., 2017; Fang et al., 2018). However, the relationship between climatic factors and EVI may differ over different regions and times. For example, Sun et al. (2015) reported that significant and positive partial correlations between temperature and the NDVI were found in the central and southeastern Loess Plateau, while a negative impact of vegetation degradation due to climate warming occurred in the northwestern Loess Plateau. Wen et al. (2017) found that rising temperature was the primary contributor of NDVI increase before 1990s, and decreasing precipitation was the main climatic factor

influencing the mid-western farmland areas' NDVI variations after 1990s.

Traditional way to quantifying vegetation cover mostly depends on field survey, which is advanced in high accuracy but time and human resources consuming (Wen et al., 2010). With the development of remote sensing, satellites provide valuable data resources for assessing land cover change (Giri et al., 2007; Bartholomé and Belward, 2005). To date, many satellite sensors have been used to detect land cover change over large areas, such as Moderate-Resolution Imaging Spectroradiometer (MODIS, 250 m/500 m), the System Pour l'Ovseration de la Terre (SPOT, 1 km), Sea-Viewing Wide Field-of-View Sensor (SeaWiFS, 4.63 km) and the Advanced Very High Resolution Radiometer (AVHRR, 8 km) (Lamchin et al., 2017; Zhang et al., 2018;). However, these sensors are in coarse resolution, failing to capture the finer and more local characteristics of vegetation cover change, which are highly needed in local ecosystem services and assessment especially for urban or suburban areas.

Alternatively, Landsat (including Landsat 5, 7 and 8) provides an ideal option with a fine spatial resolution of 30 m and temporal resolution of 16 days. It allows for monitoring human-included land cover change (Huang et al., 2010; Zhu et al., 2016) and evaluating the vegetation cover change on local or regional scale (Zhu et al., 2016; Jönsson et al., 2018; Restrepo et al., 2017).

In remote sensing-based vegetation cover study, various vegetation indices (VIs) have been proposed to represent vegetation cover. Particularly, normalized difference vegetation index

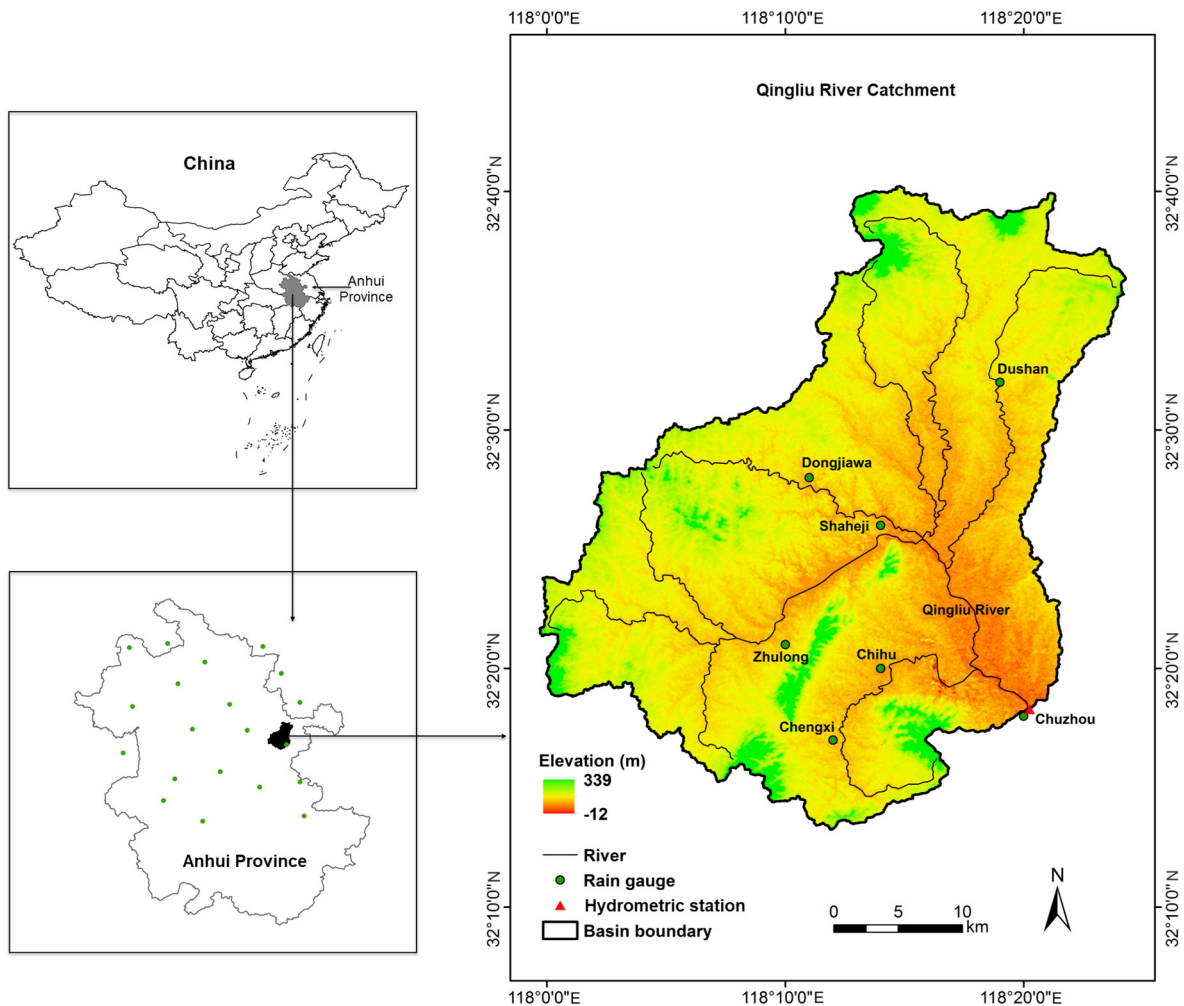


Fig. 1. Location, elevation, and distribution of hydro-meteorological stations in the Qingliu River catchment, southeast China.

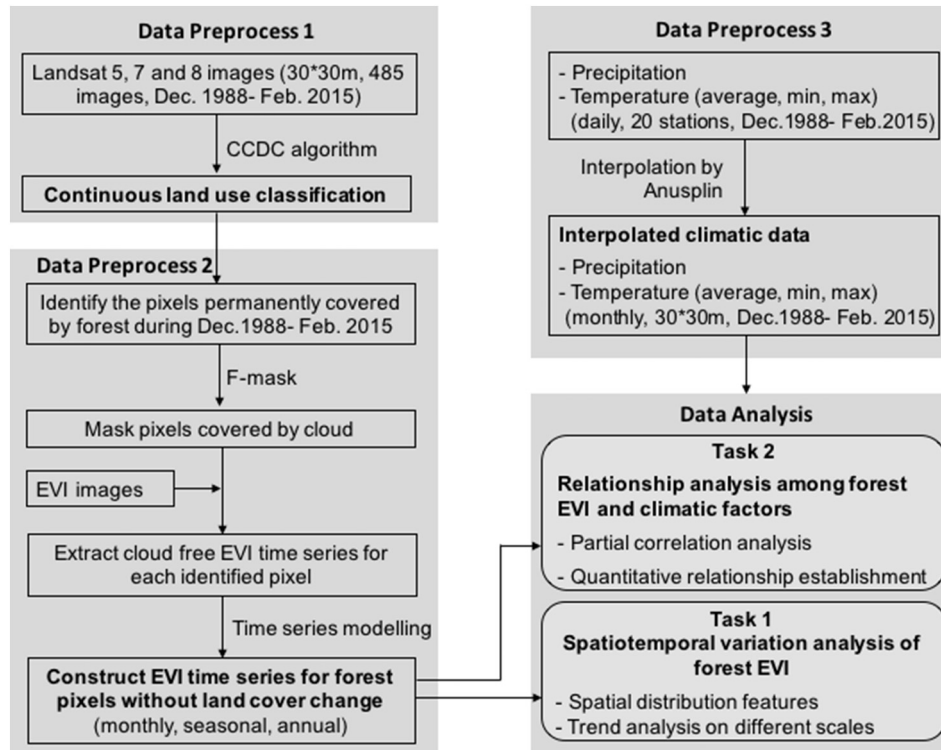


Fig. 2. Flowchart of the framework.

(NDVI) and enhanced vegetation index (EVI) are widely used due to their high correlation with the amount of chlorophyll, vegetation leaf area, and photosynthetic capacity (Carlson and Ripley, 1997; Olofsson et al., 2007). In contrast with NDVI, EVI is generally more robust to the influences of atmosphere and soil background and is less sensitive to saturation problems over dense canopies (Huete et al., 2002). In addition, comparing the consistency of data from Landsat 8 with Landsat 5 and 7, Zhu et al. (2016) found that the EVI values were less biased than that of NDVI and suggested use EVI data for vegetation change analysis without further calibration. Therefore, EVI is selected to represent forest coverage in this study.

### 1.2. The impacts of human activities and climate change on vegetation cover

Land cover change can be broadly attributed to climate change and human activities (such as deforestation, urban expansion). In recent decades, increasingly intensive human activities have disturbed land cover dramatically and even become the dominant driver of land cover change especially for urban or suburban areas (Vitousek et al., 1997; Yin et al., 2018). In this case, land cover change induced by human activities may either accelerate or counteract the response of vegetation to climate change (Theurillat and Guisan, 2001). Thereby, the response of vegetation cover to climate change may be very different if the effects of human activities are not excluded (Zhu et al., 2016; Shen et al., 2018). However, most studies on the impact of climate change on vegetation cover variation assume that there is no land cover change or a little change occurs but can be ignored (Luo and Yu, 2017). Apparently, the above assumption fails to hold in the real world especially for long time intervals, or for areas that undergo substantial land cover changes (Restrepo et al., 2017). Therefore, the effects of land cover change induced by human activities should be excluded when we assess the impact of climate change on vegetation variation.

How to achieve the objective? One option is identifying areas where are consistently covered by the same type of vegetation. To tackle this

problem, Zhu and Woodcock (2014) proposed a robust algorithm named Continuous Change Detection and Classification (CCDC) of land cover by using all available Landsat data. It allows for producing land cover classification result at any time in the given study period. The CCDC algorithm has been adopted in a new U.S. Geological Survey (USGS) science initiative named Land Change Monitoring Assessment and Projection (LCMAP, 2018).

In this study, based on all available Landsat 5, 7 and 8 imageries, the CCDC algorithm is applied to get the continuous classification of land cover in the Qingliu River catchment during 1989–2014. Subsequently, the pixels that are permanently covered by forest over the study period are identified for further study. It is important to note that since farmland are substantially impacted by human activities such as harvesting or feeding, only forest cover is focused in this study.

### 1.3. Aims and objectives

This paper aims to assess the impact of climate change on forest cover with human-induced land cover change effect excluded. Taking the Qingliu River catchment, which undergoes substantial land use changes, as a case study, the objectives are as follows:

- 1) To detect land cover change and produce continuous land cover classification for the study area;
- 2) To analyze the spatial distribution and temporal trend characteristics of forest cover driven by climate change on different scales;
- 3) To explore the relationships among forest coverage (represented by EVI) and climatic factors.

## 2. Study area and data acquisition

### 2.1. Study area

The Qingliu River is a secondary-order tributary of the downstream of Yangze River, flowing towards southeast and joining in Chu River at

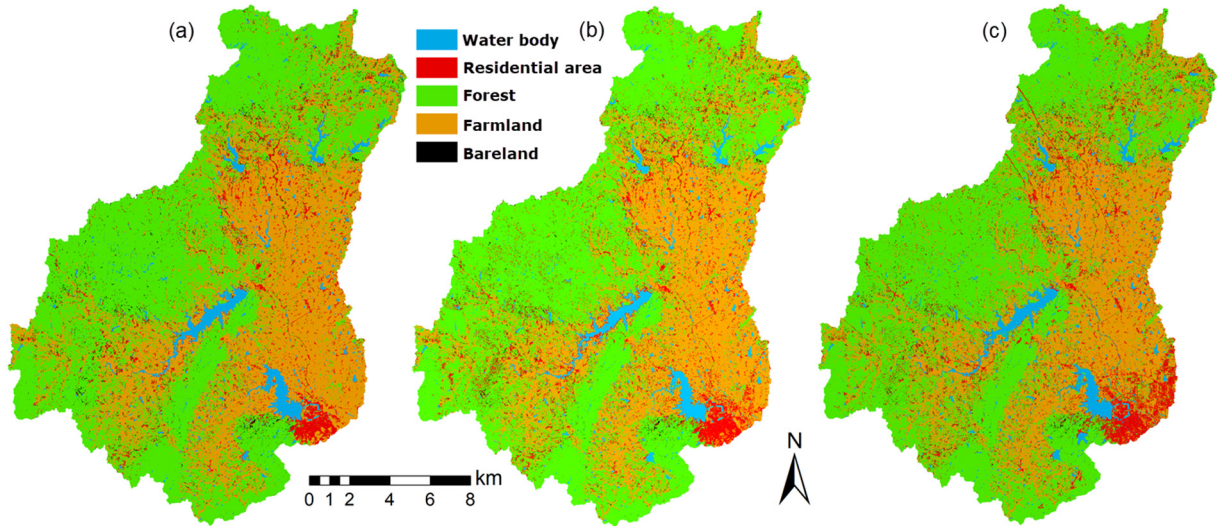


Fig. 3. Land cover classification of the Qingliu River catchment in January 1989 (a), January 2001 (b), and January 2015 (c), respectively.

Chuzhou station. The Qingliu River catchment (32.22°–32.67° N, 117.99°–118.40° E, Fig. 1) belongs to transition zone (31.4°N and 35.2°N) between Southern China and Northern China, where there exists complex relationship between vegetation and climate change (Luo and Yu, 2017). Located in the subtropical humid monsoon region, the catchment covers a drainage area of 1318 km<sup>2</sup>, receives a mean annual precipitation of about 1100 mm and is subject to a mean temperature of 15.2 °C. The elevation of the catchment ranges from –12 m to 339 m, is a representative area for southeastern low mountains and hills in China (Yang et al., 2019).

The land cover in the study area is dominated by farmland and forest. Only a small proportion of grassland has been noted. But in recent decades, the catchment undergoes substantial land cover changes (mainly shifting from farmland and forest to residential area) due to the rapid development of society and economy (Liu et al., 2010; Zhang and Pu, 2008).

2.2. Data acquisition

In seasonal variation analysis, data in winter referring to January and February in the next year are needed. Hence, data covering the period of December 1988–February 2015 are collected and analyzed in this study.

2.2.1. Climatic data

The daily data of mean temperature (Tmean), minimum temperature (Tmin), maximum temperature (Tmax), and precipitation ranging from December 1988 to February 2015 for 20 meteorological stations (Fig. 1, 1 station within the catchment and 19 stations around the catchment) are acquired from the China Meteorological Administration (CMA, http://data.cma.cn/). Since a large proportion of daily pan-evaporation data provided by CMA are missing, monthly pan-evaporation in the study area is collected from Anhui Meteorological Bureau. Monthly precipitation data of 7 rain gauges were provided by Anhui Hydrology Bureau.

Table 1  
Proportion of each land cover type over the Qingliu River catchment in January 1989, January 2011, and February 2015, respectively.

	Forest	Farmland	Residential area	Water body	Bare land
Jan. 1989	53.48%	36.44%	5.18%	3.90%	1.00%
Jan. 2001	52.69%	35.01%	7.53%	3.96%	0.82%
Jan. 2015	53.32%	34.01%	7.55%	4.42%	0.70%

2.2.2. Landsat data, EVI data and DEM

All available Level 1 Terrain (L1T) Landsat 5, 7 and 8 images of the study area with cloud cover <90% from December 1988 to February 2015 are downloaded from United States Geological Survey (USGS, https://earthexplorer.usgs.gov/). The total number of all available Landsat images from Thematic Mapper (TM) on Landsat 5, Enhanced Thematic Mapper Plus (ETM+) on Landsat7, and Operational Land Imager (OLI) on Landsat 8 is 485 and the number of images in each year from 1989 to 2014 is listed in Table S1 in supplement files. Since before 2000 there is only Landsat5 (TM) while after 2000 there are both Landsat5 (TM) and Landsat7 (ETM), therefore the quantity of images before 2000 is less than that after 2000.

Correspondingly, EVI images covering the same time period are also downloaded from USGS (https://earthexplorer.usgs.gov/). These images have been corrected by calibration, view geometry, volcanic aerosols, and other effects that have no relation with vegetation change (Pinzon and Tucker, 2014). The frequency by month of all available EVI datasets for the study area is listed in Table S2 in supplement files. The months during the growing season (April–October) have slightly more images than the other months.

DEM data with a spatial resolution of 30\*30 m are downloaded from Geospatial Data Cloud in China (http://www.gscloud.cn/). High definition images of GF-1 with a resolution of 2\*2 m are provided by China Center for Resources Satellite Data and Application.

3. Methodology

3.1. Overview of the framework

Fig. 2 illustrates the flowchart of the framework, which consists of two modules: data preprocess and data analysis. Specifically, data preprocess includes three parts, namely land cover dynamics exploration (data preprocess 1 in Fig. 2, refer to Section 3.2), EVI time series construction of the forest pixels without land cover change (data preprocess 2 in Fig. 2, refer to Section 3.3), and climatic data interpolation (data preprocess 3 in Fig. 2, refer to Section 3.4). Data analysis covers two tasks: (1) spatiotemporal variation analysis of forest EVI; and (2) Relationship analysis among EVI and climatic factors. The related methods and techniques used in data analysis are introduced in Section 3.5.

3.2. Exploration of land cover dynamics

The Continuous Change Detection and Classification (CCDC) algorithm, originally designed for Landsat data, is a robust methodology

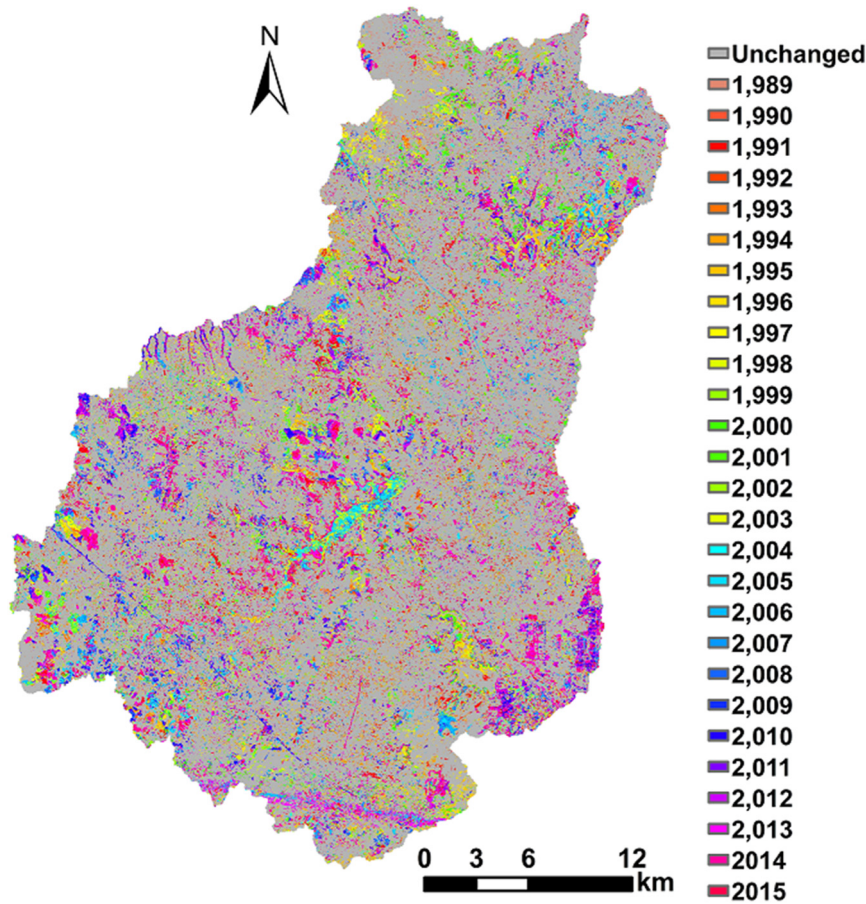


Fig. 4. Land cover change map for the Qingliu River catchment between 1989 and 2014 relative to land cover in December 1988.

for identifying when and how a land surface pixel changes through time by using all available Landsat imagery (Zhu and Woodcock, 2014).

The CCDC algorithm mainly consists of four steps: (1) image pre-processing, where atmospheric correction is operated; clouds, clouds shadows, and snow are initially masked using F-mask algorithm (Zhu et al., 2015). (2) Time series modelling (Eq. (1)), aiming to capture the characteristics of intra-annual change, gradual inter-annual change and abrupt change of land surface. (3) Change detection, which compares predictions mathematically to observations to determine whether change has occurred at any given time. (4) Land cover classification, performed by using the Random Forest Classifier (RFC) due to its high accuracy and computational efficiency (Rodriguez-Galiano et al., 2012).

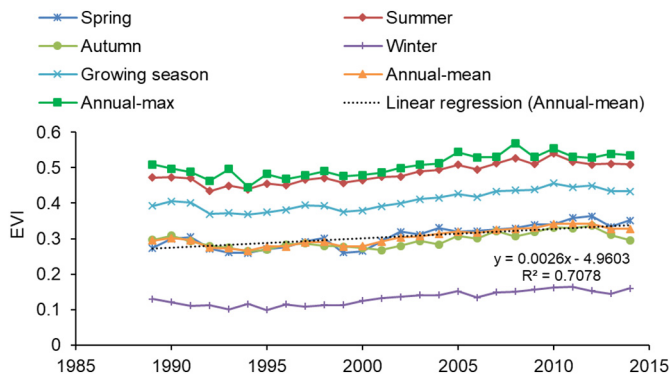


Fig. 5. Inter-annual change trends of seasonal and annual EVI in the Qingliu River catchment during 1989 and 2014.

$$\hat{\rho}(i, x)_{OLS} = a_{0,i} + a_{1,i} \cos\left(\frac{2\pi}{T}x\right) + b_{1,i} \sin\left(\frac{2\pi}{T}x\right) + c_{1,i}x \quad (1)$$

$$\{\tau_{k-1}^* < x \leq \tau_k^*\}$$

where  $x$ : Julian date;  $i$ : the  $i$ th Landsat Band;  $T$ : number of days per year ( $T = 365$ );  $a_{0,i}$ : coefficient for overall value for the  $i$ th Landsat Band;  $a_{1,i}$ ,  $b_{1,i}$ : coefficient for intra-annual change for the  $i$ th Landsat Band;  $c_{1,i}$ : coefficient for inter-annual change for the  $i$ th Landsat Band;  $\tau_k^*$ : The  $k$ th break points;  $\hat{\rho}(i, x)_{OLS}$ : predicted value for the  $i$ th Landsat Band at Julian date  $x$ .

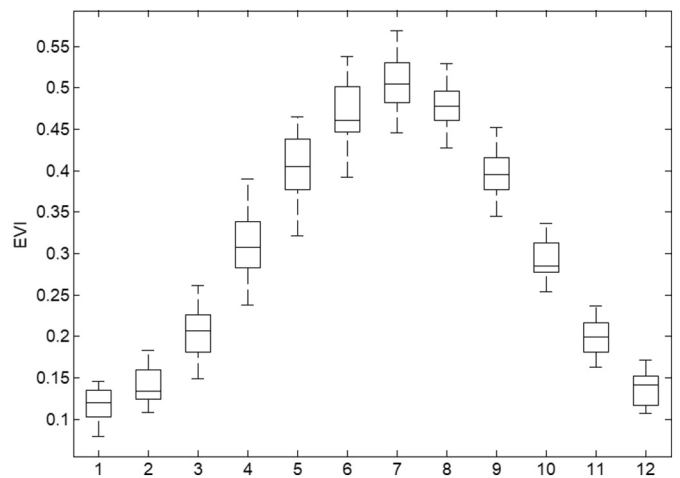
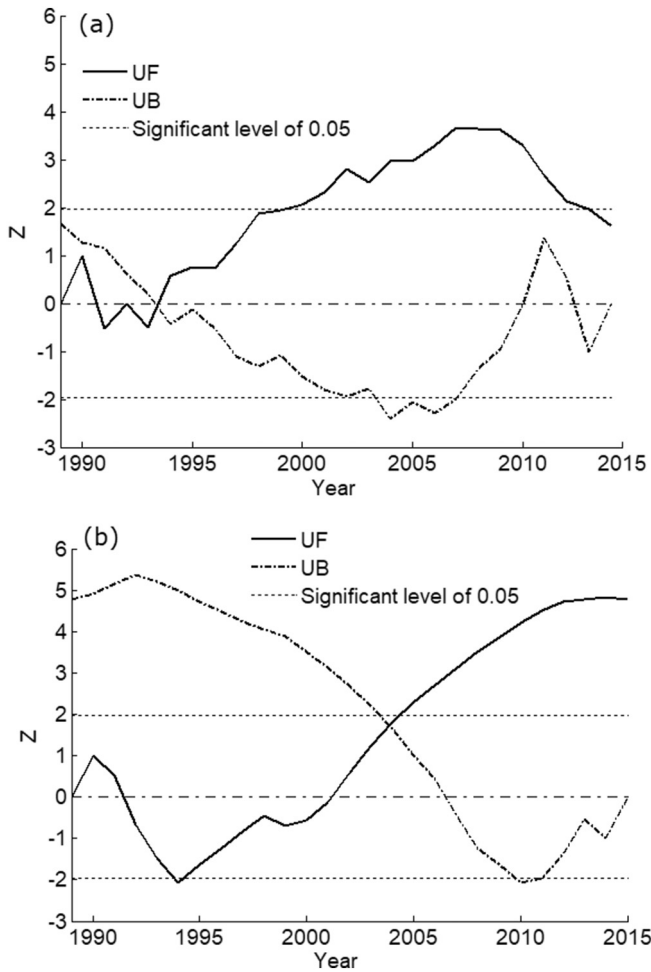


Fig. 6. Box-whisker of intra-annual change of EVI in the Qingliu River catchment over the period of 1989 and 2014. The bottom and top of the box are the first and third quartiles, and the band inside the box is the median. The “whisker” above and below the box represents the maximum and minimum of all data. The same hereafter.



**Fig. 7.** Change detection of mean annual temperature (a) and EVI (b) during 1989 and 2014. UF and UB present the forward trend and backward trend line of the data series.  $UF > 0$  and  $UF < 0$  indicate increasing trend and decreasing trend, respectively.

In this study, CCDC algorithm is applied for continuous classification of land cover for the Qingliu River catchment during December 1988 and February 2015. Briefly, land cover in the Qingliu River catchment is classified into five types, namely water body, forest, farmland, residential area, and bare land. In total 4215 sample points covering five types of land cover were identified (Fig. S1 in the supplement files) based on filed survey, the high definition image of GF-1 and the cloud-free Landsat images. Half of the sample points were used for training and another half were used for validation in the Random Forest Classifier.

**Table 2**  
Trend statistics of seasonal and annual EVI in the Qingliu River catchment.

	1989–2000	2001–2014	1989–2014	
	Slope (/10a)	Slope (/10a)	Slope(/10a)	$Z_{MK}$
Spring	−0.011	0.038**	0.036**	4.85**
Summer	−0.001	0.031**	0.031**	4.72**
Autumn	−0.019	0.035**	0.017**	2.95**
Winter	−0.004	0.019**	0.022**	4.72**
Growing season	−0.011	0.037**	0.030**	4.63**
Annual-mean	−0.011	0.031**	0.026**	4.81**
Annual-max	−0.017	0.032*	0.031**	3.92**

Note: \*\* and \* mean significance levels ( $\alpha$ ) of 0.01 and 0.05, respectively. The corresponding values of  $Z_{1-\alpha/2}$  are 2.32 and 1.96, respectively. Positive  $Z_{MK}$  indicates increasing trend, while negative  $Z_{MK}$  indicates decreasing trends. If  $|Z_{MK}| > Z_{1-\alpha/2}$ , then a significant trend exists in the time series.

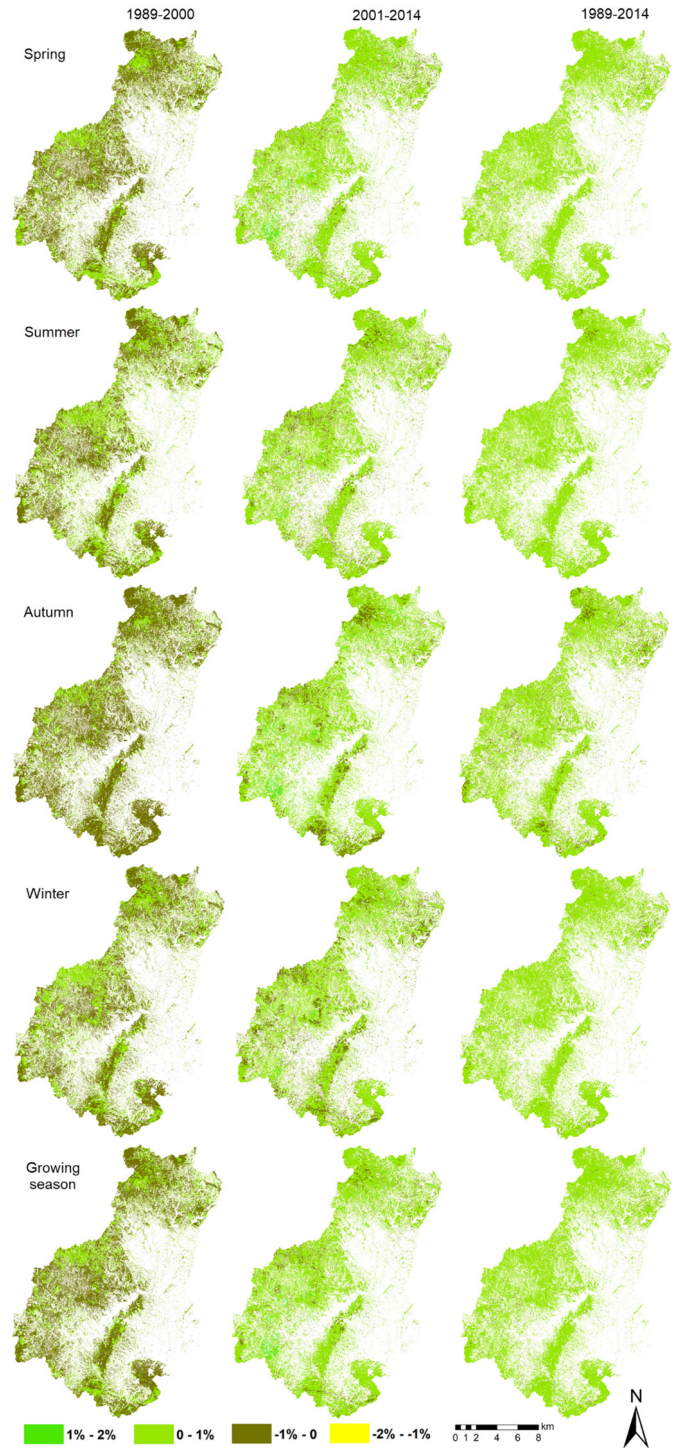


**Fig. 8.** Change trend of seasonal EVI on pixel scale in the Qingliu River catchment based on simple linear trend method over three phases (1989–2000, 2001–2014, and 1989–2014).

### 3.3. Construction of continuous EVI time series

Based on the continuous land cover classification results, pixels permanently covered by forest over the period of Dec. 1988–Feb. 2015 are identified as our research objects. Forest pixels which experience human induced land cover change (including transition from forest to other land cover types and from other land cover types to forest) are left out of our study objects. In this manner, the influences of human-induced land cover change on forest coverage can be removed, which

**Table 3**  
Statistics of individual change rates of EVI in the Qingliu River catchment.

		-2%–1%/a	-1%–0/a	0–1%/a	1%–2%/a
Spring	1989–2000	0.2%	66.0%	33.7%	0.1%
	2001–2014	0.1%	10.5%	85.7%	3.7%
Summer	1989–2014	/	3.9%	96.1%	/
	1989–2000	0.1%	53.2%	46.3%	0.4%
Autumn	2001–2014	0.3%	14.4%	83.5%	1.8%
	1989–2014	/	2.3%	97.7%	/
Winter	1989–2000	0.3%	77.2%	22.5%	/
	2001–2014	0.2%	14.4%	80.1%	5.3%
Growing season	1989–2014	/	12.2%	87.8%	/
	1989–2000	/	56.8%	43.1%	0.1%
Annual	2001–2014	0.1%	22.9%	75.8%	1.2%
	1989–2014	/	4.2%	95.8%	/
Annual	1989–2000	0.2%	66.2%	33.5%	0.1%
	2001–2014	0.2%	10.0%	85.9%	3.9%
Annual	1989–2014	/	3.6%	96.4%	/
	1989–2000	0.1%	68.0%	31.8%	0.1%
Annual	2001–2014	0.1%	12.5%	85.2%	2.2%
	1989–2014	/	3.7%	96.3%	/

Note: The total number of identified forest pixel is 496,559. /a means per year.

means the variations of these forest pixels are mainly derived from climate change.

For each identified forest pixel, the EVI time series can be extracted from all the available EVI imagery. To avoid the cloud and snow effects,

pixels with cloud, cloud shadows and snow are further masked by using F-mask algorithm (Zhu et al., 2015) from individual EVI images. As a result, cloud free EVI time series are constructed for each identified pixel. Due to the fact that EVI imagery is not always at 16-day interval, a time series model (Eq. (1)) proposed by Zhu and Woodcock (2014), which takes the seasonal variation feature of EVI into account, is applied to fit available EVI to get continuous EVI data. Finally, monthly EVI time series for each identified pixel are constructed.

### 3.4. Interpolation of climatic data based on ANUSPLIN

To analyze the correlation between forest EVI and climatic variables on pixel scale, climatic data with the same spatial resolution of EVI need to be interpolated. ANUSPLIN, as a professional interpolation software for meteorology data, has been widely used worldwide (Hutchinson and Xu, 2004; Tan et al., 2018). The spline interpolation method from ANUSPLIN has shown its superiority on monthly climate data interpolation in China (Hong et al., 2010). Hence, based on DEM (30\*30 m) and the climatic data at 20 meteorological stations (Fig. 1), ANUSPLIN (Hutchinson and Xu, 2004) is applied to interpolate climatic variables (i.e. precipitation, Tmean, Tmin, Tmax) at a pixel size of 30 m for Anhui province on monthly and annual scales, respectively. As a result, monthly temperature and precipitation during December 1988 and February 2015 and annual temperature and precipitation during 1989–2014 on pixel scale are constructed.

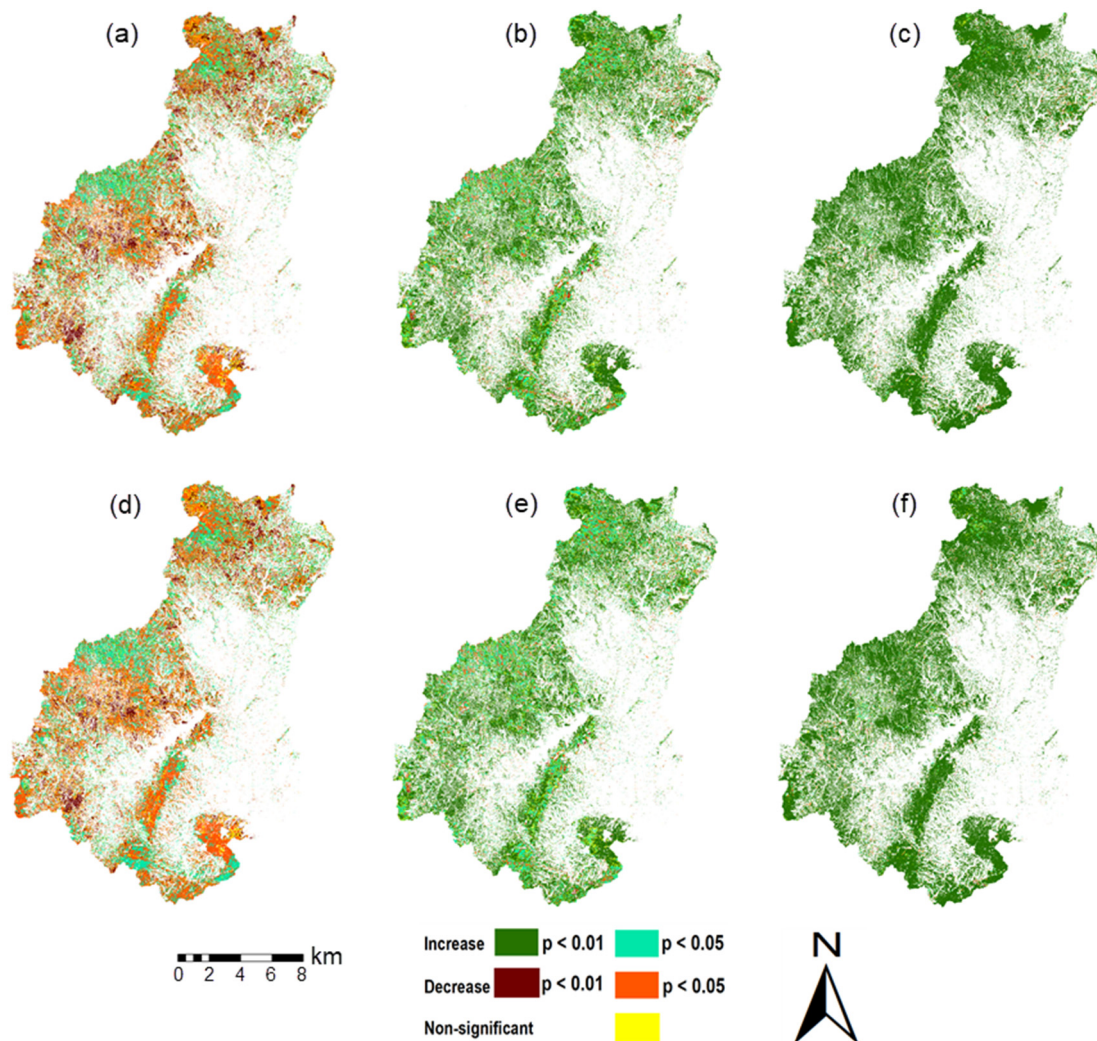


**Fig. 9.** Significance of EVI change on pixel scale in the Qingliu River catchment. (a)–(c): Significance of annual EVI change during 1989–2000, 2001–2014, 1989–2014, respectively; (d)–(f) Significance of change of EVI in growing season during 1989–2000, 2001–2014, 1989–2014, respectively.

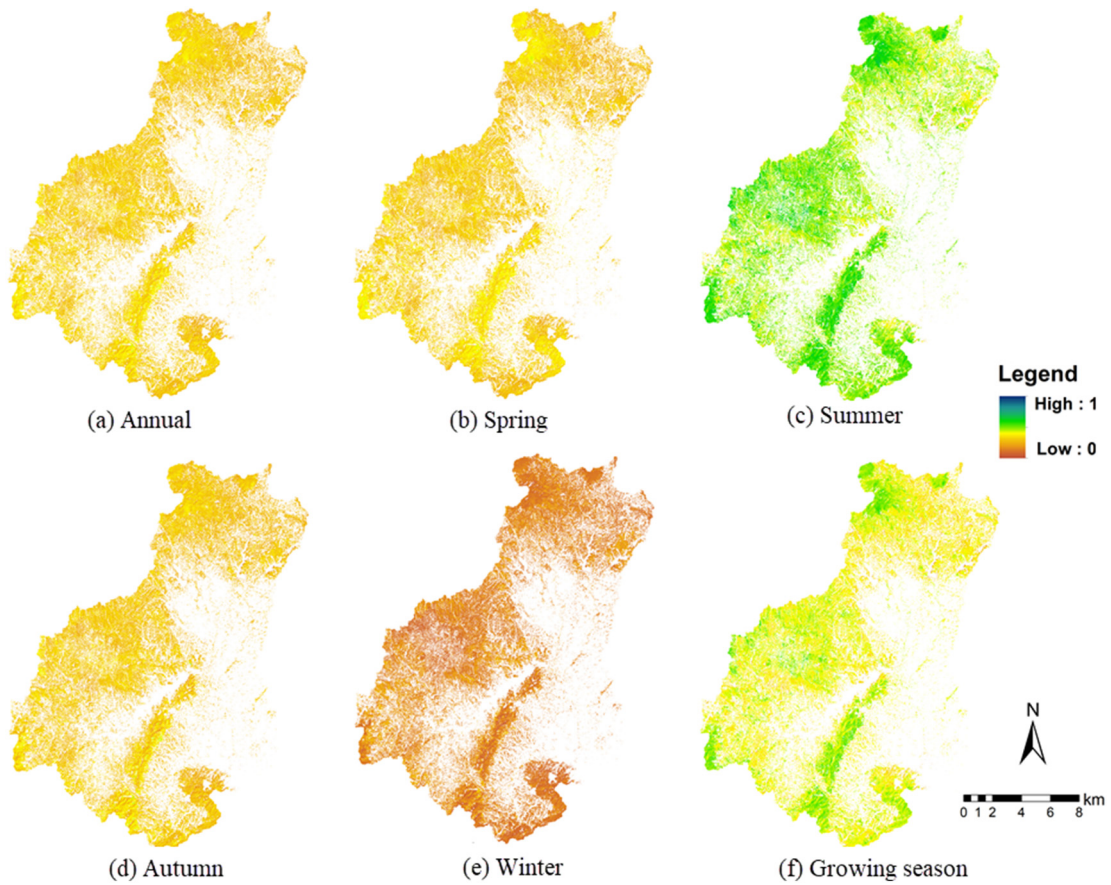


Fig. 10. Spatial distribution of annual and seasonal EVI in the Qingliu River catchment over the period of 1989 and 2014.

3.5. Data analysis

3.5.1. Spatiotemporal variation analysis of forest EVI

Diverse methods of spatiotemporal variation analysis have been proposed (Yang et al., 2017). In this study, to characterize the spatial variation features of forest EVI, spatial heterogeneity of seasonal and annual EVI over three different phases are displayed and compared. To

analyze the temporal trends of forest EVI, a simple linear trend (SLT) method and Mann-Kendall (MK) test method (Mann, 1945; Kendall, 1975) are selected. SLT method works well for areas where not undergoing substantial land cover change (Zhu et al., 2016). MK test is a robust non-parametric method that have been widely applied in detecting monotonic trends in climate, hydrology and vegetation coverage (Shadmani et al., 2012; Torres and Moisés, 2013; Zuo et al., 2016).

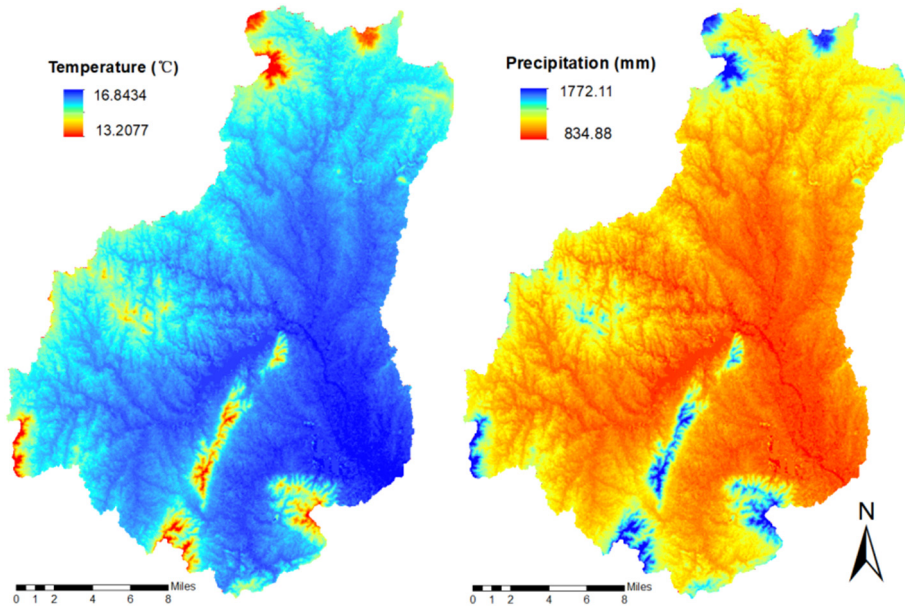


Fig. 11. Mean annual temperature and precipitation in the Qingliu River catchment during 1989 and 2014.

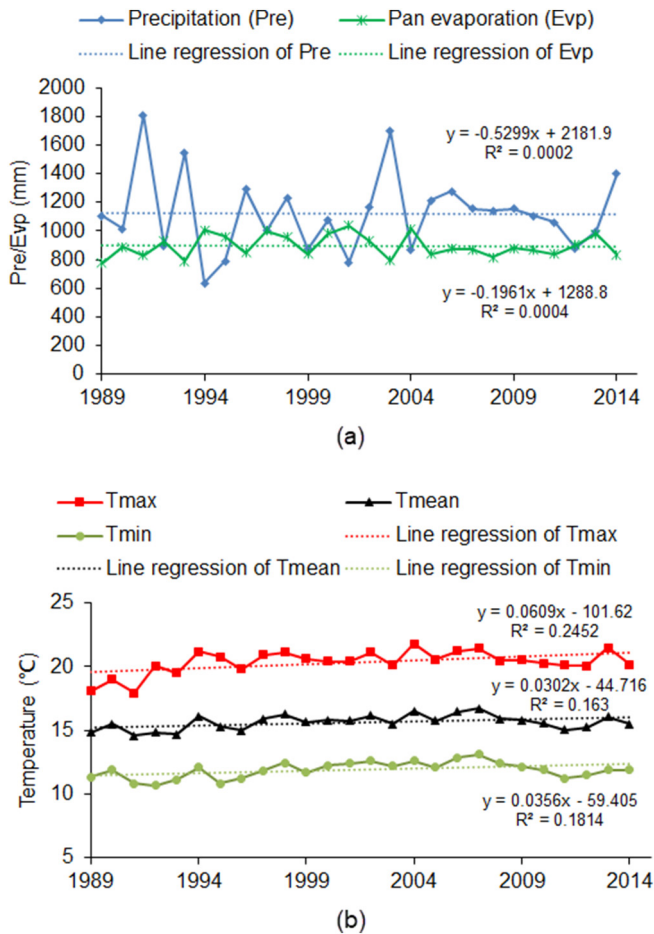


Fig. 12. Inter-annual change trends of mean annual precipitation, pan evaporation (a) and temperature (b) for the Qingliu River catchment during 1989 and 2014.

### 3.5.2. Relationship analysis among EVI and climatic factors

To evaluate the correlation among climatic factors and forest EVI, partial correlation analysis is selected, which measures the strength of a relationship between two variables while eliminating the effects of correlated one or more control variables (Wu et al., 2015).

The partial correlation coefficients can be written as follows (Eq. (2)):

$$r_{XY:Z} = \frac{r_{XY} - r_{XZ}r_{YZ}}{\sqrt{(1-r_{XZ}^2)(1-r_{YZ}^2)}} \quad (2)$$

where  $r_{XY:Z}$  means the partial correlation between  $X$  and  $Y$  given a set of  $n$  controlling variables  $Z = \{Z_1, Z_2, \dots, Z_n\}$ .  $r_{XY}$ ,  $r_{XZ}$ ,  $r_{YZ}$  represent for the correlation coefficients between  $X$  and  $Y$ ,  $X$  and  $Z$ ,  $Y$  and  $Z$ , respectively. In this study,  $X$  denotes forest EVI,  $Y$  denotes one of climatic factors (temperature, precipitation, pan-evaporation),  $Z$  denote for another two climatic factors.

Like the correlation coefficient, the partial correlation coefficient (PCC) also ranges from  $-1$  to  $1$ . PCC with the value of  $-1$  or  $1$  means a perfect negative or positive correlation controlling for some variables and PCC with the value of  $0$  conveys that there is no linear relationship (Epskamp and Fried, 2018).

The partial correlations among EVI and climatic factor are analyzed on different spatial scales (pixel and catchment) and temporal scales (monthly, seasonal and annual). Finally, their quantitative relationship is established via least square method (Rehman et al., 2017).

## 4. Results and discussion

### 4.1. Continuous change detection and classification of land cover in the Qingliu River catchment

Based on all the available Landsat imagery in the study area and the CCDC algorithm, the continuous changes of land surface are detected and the dynamic land cover classifications during December 1988 and February 2015 are generated.

Due to the continuity of the land cover classification, it is unrealistic to show all the classification results and the associated accuracies. Table S3 lists the mean accuracy of land cover classification in each month during 1989–2014. It indicates that the overall mean accuracy achieves over 90%, which provides quality assurance for the subsequent analysis.

Taking the land cover in January 1989, January 2001, and January 2015 as examples, Fig. 3 and Table 1 show their corresponding classification results. It is obvious that the residential area has expanded with the development of economy and society in last 26 years, while farm land and forest have been shrinking and are mainly replaced by residential areas.

Although Fig. 3 and Table 1 present land cover changes between January 1989 and January 2015, they cannot track and reveal the change dynamics (e.g. when and where does the change happen). Alternatively, Fig. 4 illustrates the land cover changes in each year during the period of 1989 and 2014 relative to December 1988. Different colors represent for the changed pixels in different years. The “unchanged” bar in the legend means the areas which have no use change occurred.

Based on the continuous land cover classification results, the statistical data indicate that 28.1% of the study area undergoes land cover change. Furthermore, compared with forest proportion in December 1988, 22.07% of the forest area has experienced land cover changes, including both deforestation and reforestation by human activities. Therefore, human-induced forest change should be excluded when studying the impact of climate change on forest coverage variation. As a result, here we identify the pixels (with the number of 495,477) which are permanently covered by forest over the study period for further analysis. The identified pixels account for 41.77% of the Qingliu River catchment with the total number of pixels of 1,188,812.

### 4.2. Spatiotemporal variation of forest cover in the Qingliu River catchment

#### 4.2.1. Temporal trend analysis of forest EVI

4.2.1.1. On catchment scale. To represent forest EVI level on catchment scale, EVI of all identified forest pixels are averaged. Subsequently, the inter-annual and intra-annual variations of the EVI are presented in Figs. 5 and 6, respectively.

Fig. 5 illustrates the change trends of annual EVI (including mean annual and maximum annual) and seasonal EVI in the Qingliu River catchment during 1989 and 2014. In general, EVI increases and individual change trends are consistent with each other. To evaluate the intra-annual variation of EVI, box-whiskers plot was provided in Fig. 6, where the median indicates the middle value, and the bottom and top of the box characterize the variation. It can be found that EVI achieves the highest value in July and lowest value in December and January. The finding is consistent with seasonal features of vegetation phenology.

Based on the Mann Kendall method, changes of mean annual temperature and EVI were detected and the results are illustrated in Fig. 7. It can be noted that temperature abruptly changed in 1994 and increased significantly since 2000 (Fig. 7(a)), and EVI abruptly changed in 2004 (Fig. 7(b)). It might because the effect of climate change is lagged and accumulated on forest cover. To further investigate the climate impact on forest cover, we consequently separate the whole study period into two segments by taking 2000 as the break point,

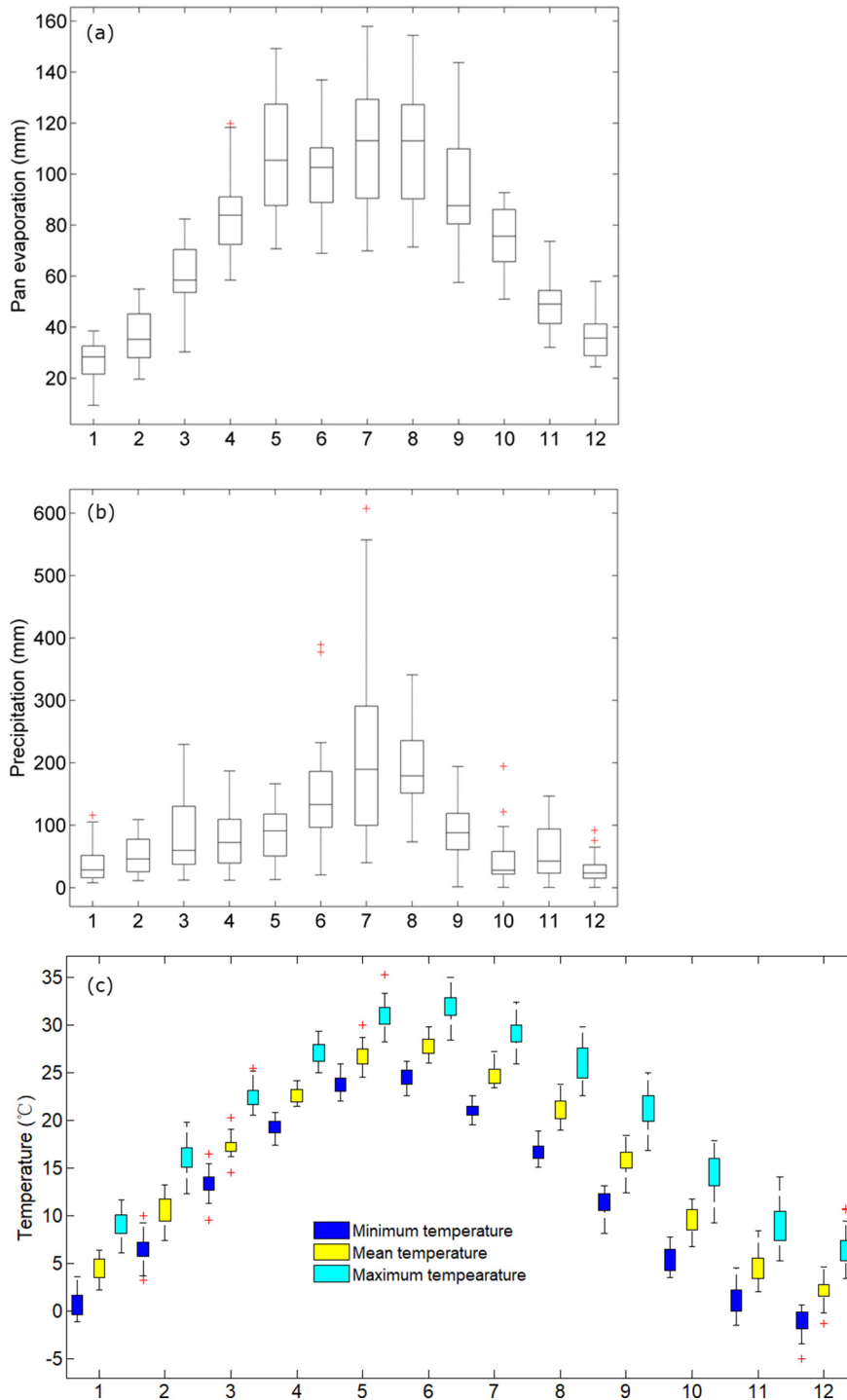


Fig. 13. Box-whisker of intra-annual change of pan evaporation (a), precipitation (b), and temperature (c) in the Qingliu River catchment during 1989 and 2014.

namely 1989–2000 and 2001–2014. In addition, EVI exhibits distinct seasonal characteristic. Thereby, we look into temporal change of EVI from seasonal and annual levels over three phases (1989–2000; 2001–2014; 1989–2014) (Table 2). Here, spring refers to March to May; summer refers to June to August; autumn refers to September to November; winter refers to December, and January and February in the second year; and growing season refers to April to October.

The statistical information about the change trends of EVI over different phases is presented in Table 2. It can be observed that both annual and seasonal EVI increase significantly ( $p < 0.01$ ,  $Z_{MK} > 2.32$ ) over the entire study period, but decrease insignificantly during 1989–2000 ( $p$

$> 0.05$ ) before increase significantly ( $p < 0.01$ ) over the period of 2001–2014.

4.2.1.2. On pixel scale. For each identified pixel which is permanently covered by forest, the simple linear trend (SLT) method is used on its EVI time series data. Here, the slope coefficient represents the change rate of EVI. Fig. 8 shows the spatial distribution of change rates of seasonal EVI over three different phases across the Qingliu River catchment. Statistical information of these changes is summarized in Table 3.

From Fig. 8 and Table 3, we can find key findings as follows: (1) EVI degradation during 1989–2000 accounts for 68.1% (53.3%–77.5%), EVI

**Table 4**  
Partial correlation coefficients among forest EVI and climatic variables on different time scales over the catchment.

	EVI-Pre	EVI-Tmax	EVI-Tmean	EVI-Tmin	EVI-Evp
Spring	0.233	0.203	0.262	0.222	0.192
Summer	-0.053	0.583**	0.737**	0.766**	-0.720**
Autumn	-0.158	-0.029	0.008	0.049	-0.400
Winter	-0.431*	0.133	0.104	0.107	-0.485*
Growing season	0.061	0.415*	0.523**	0.523**	-0.354
Monthly	0.317 g**	0.739**	0.793**	0.798**	0.017
Annual	-0.068	0.348	0.399	0.409*	-0.368

Note: EVI: enhanced vegetation index; Pre: precipitation; Tmin: minimum temperature; Tmean: averaged temperature; Tmax: maximum temperature; Evp: Pan evaporation. \* and \*\* represent significance levels of 0.05 and 0.01, respectively. PCC > 0 means positive correlation between EVI and the climatic variables, while PCC < 0 indicates negative correlation.

increasing during 2001 and 2014 accounts for 87.4% (77.0%–89.8%), and EVI increasing over the whole study period account for 96.3% (87.8%–97.7%). These change trends on pixel scale are consistent with that found on catchment scale. Furthermore, it indicates that the spatial distribution of EVI is largest during 1989–2000, followed by 2001–2014. (2) No matter for increases or decrease, majority (over 90%) of the change magnitude is around 1%/year. Pixels showing changes with larger magnitude of 1–2%/year are much fewer or negligible. It can be explained that since climate fluctuates gradually in certain extent, thus forest cover driven by climate also varies in a relative small magnitude. (3) For each phase, the largest proportion of decreasing appears in autumn or winter, while its largest proportion of increasing appears in summer or spring. For instance, during 1989–2000, the largest proportion of EVI degradation is in autumn with 77.2% and highest proportion of EVI increasing is in spring with 85.7%. This might because forest starts the growing season in spring and achieves highest EVI in summer. While in autumn and winter, the forest gets closer to the end of growing season. The findings are consistent with the phenological characteristics of forest.

To investigate whether EVI change is significant or not, *p*-value generated from simple linear trend for pixel EVI over three different phases is analyzed and visualized in Fig. 9. The upper part of Fig. 9 shows the significance of annual EVI change while the bottom part of Fig. 9 represents the significance of EVI change in growing season. In general, we can observe that annual and seasonal EVI in a large proportion (>80%) of forest pixels change significantly. Taking growing seasonal EVI as an example, 86.0% of the forest pixels change significantly ( $p < 0.05$ ) during 1989–2000, while EVI changes very significantly during 1989–2014 and

2001–2014, accounting for 55.8% and 97.2%, respectively. More detailed statistical information can be found in Table S4.

#### 4.2.2. Spatial distribution of forest EVI

The spatial distribution of mean annual and seasonal EVI during 1989–2014 is illustrated in Fig. 10. In combination with river system and DEM in Fig. 1, it can be noticed that most forest is distributed in boundary regions (which are also river sources regions) or middle ribbon areas of hills. Hence, EVI spatial distribution is highly associated with elevation. The spatial distribution of EVI differs on different seasonal scales over different phases. For different seasons, substantial spatial distribution can be observed in summer and growing season. Similar findings can be found over another two phases (1989–2000 and 2001–2014), which can be found in Figs. S2 and S3 in supplement files.

#### 4.3. Relationship among EVI and climatic factors on different scales

##### 4.3.1. Spatial distribution and temporal variation of climatic factors

The spatial heterogeneities of mean annual temperature and precipitation in the study area over the years of 1989–2014 are illustrated in Fig. 11. In comparison with DEM in Fig. 1, it can be noted that the areas with low temperature, high precipitation and high elevation are highly consistent with each other. These areas are mainly located in northern, southern boundary or middle hills of the Qingliu river catchment.

The temporal changes of mean annual precipitation, pan evaporation and temperature (Tmean, Tmax, Tmin) during 1989–2014 are illustrated in Fig. 12. It indicates that both precipitation and pan evaporation change non-significantly ( $p > 0.05$ , Fig. 12(a)), while temperature increases significantly ( $p < 0.1$ , Fig. 12(b)). In addition, Fig. 13 presents the box-whisker of intra-annual change of these climate variables.

##### 4.3.2. Partial correlation analysis of EVI and climatic factors on catchment scale

Partial correlation coefficients (PCCs) among EVI, precipitation, temperature, and pan evaporation on catchment scale are summarized in Table 4. It indicates that (1) For different temporal scales, the primary climatic factors controlling EVI may differ. For instance, on summer, growing season, monthly, and annual scales, minimum temperature (Tmin) shows highest PCC with EVI, while on winter scales, pan evaporation exhibits largest PCC with EVI. However, in spring and autumn, no climatic factors show significant correlation with EVI. The results imply that pan evaporation is a primary control factor for forest cover in winter, while minimum temperature plays important roles especially on summer, monthly and annual scales. Furthermore, on monthly scale, temperature and precipitation are two dominant factors affecting forest cover. (2) For different climatic factors, their highest PCCs with EVI may appear on different scales. For example, precipitation shows its highest PCC (−0.434) with EVI on winter scale, temperature achieves the highest PCCs (0.739–0.798) with EVI on monthly scale, while pan evaporation exhibits the largest negative PCC (−0.720) with EVI on summer scale. (3) PCCs among precipitation, temperature and EVI on monthly scale are higher than those on annual scale.

To investigate the lag effect of climate on forest cover, different lags between climatic factors and forest EVI are set up and subsequently their PCCs are calculated. Here, 14 different lags are tested, namely 1 month in advance, 2 months in advance, 3 months in advance, and accumulation of 2–12 months in advance. Their corresponding PCCs are illustrated in Fig. 14. It can be observed that EVI is highly correlated with temperature in current month. Precipitation in last month (one month in advance) has higher PCC (0.343) with EVI than that in current month (0.317). Pan evaporation with two months in advance shows higher PCC (0.385) than that in current month (0.017). With the increasing of accumulation lag (2–12 months), PCCs among precipitation, pan evaporation and EVI increase gradually before falling down. Precipitation and pan evaporation achieve the highest PCCs (0.460 and 0.515, respectively)

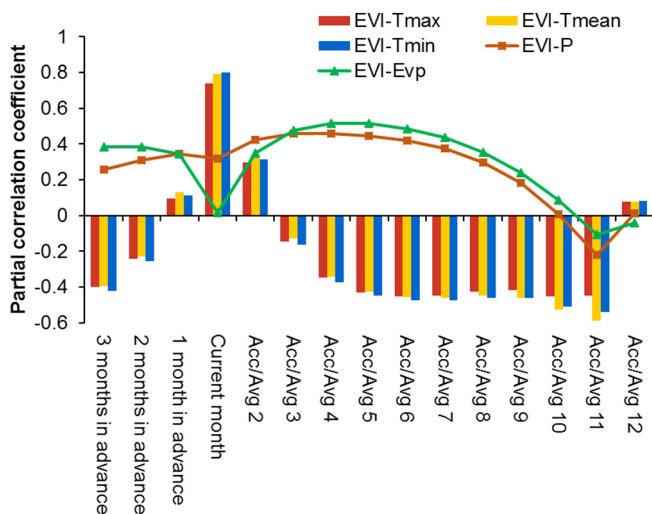


**Fig. 14.** Lag effects of climatic factors on EVI. Acc/Avg ( $i, i = 2, 3, 4, \dots, 12$ ) represents the accumulative precipitation and averaged temperature of  $i$  months.

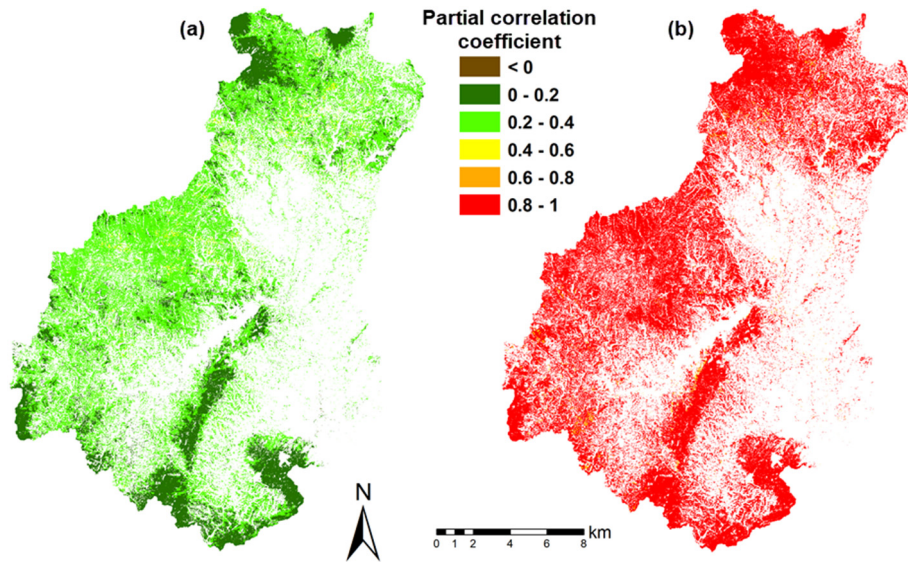


Fig. 15. Partial correlation coefficients among EVI and precipitation (a) and minimum temperature (b) on monthly scale.

with EVI at the accumulation of 4 months in advance of EVI. The results imply that precipitation and pan evaporation have lag effects (4 months) on forest EVI, while temperature has no lag effect.

4.3.3. Partial correlation analysis of EVI and climatic factors on pixel scale

Due to the lack of pan evaporation data on pixel size, here, only precipitation and temperature are used for partial correlation analysis with EVI. Besides, compared with Tmean and Tmax, Tmin shows higher PCC with EVI on both monthly and annual scales. Thereby, partial correlation analysis among minimum temperature, precipitation and EVI is finally implemented on monthly and annual scales.

Based on the mean monthly data, Fig. 15 presents the spatial distribution of partial correlation coefficients (PCCs) between EVI and precipitation as well as minimum temperature on monthly scale. In contrast, based on the mean annual data, Fig. 16 shows their PCCs on annual scale. In general, PCCs on monthly scale are higher than those on annual scale. PCCs between EVI and minimum temperature are higher than those between EVI and precipitation on both annual and monthly scales. It might partially because EVI is mainly depend on near-infrared and red bands, not as independent as precipitation (Fang et al., 2018). On the

other hand, it is consistent with existing findings that energy-limited area where vegetation cover increased generally experienced decreases in precipitation (Donohue et al., 2009).

Specifically, on monthly scale (Fig. 15), PCCs between EVI and precipitation are positive for almost all pixels, with lower PCCs (0–0.2) in high altitude areas. In contrast, EVI and minimum temperature show relative high positive PCCs over all the pixels, without large spatial difference. Statistically, 69.9% of the studied pixels exhibit that their PCCs between EVI and precipitation range from 0.2–0.4; the pixels with PCCs between EVI and precipitation lower than 0.2 account for 28.1%; pixels with PCCs between EVI and minimum temperature large than 0.8 account for 97.3%.

On annual scale, both positive and negative correlations among EVI and climatic factors (precipitation and minimum temperature) exist across the study area. Statistically, 63.0% of the pixels show that PCCs between precipitation and EVI range from 0 to 0.2; pixels with negative PCCs account for 33.6%, concentrated in areas with relatively high elevation and relatively high precipitation; the proportions of pixels with PCCs between EVI and minimum temperature in the ranges of 0.2–0.4 and 0.4–0.6 are 48.3% and 20.9%, respectively.

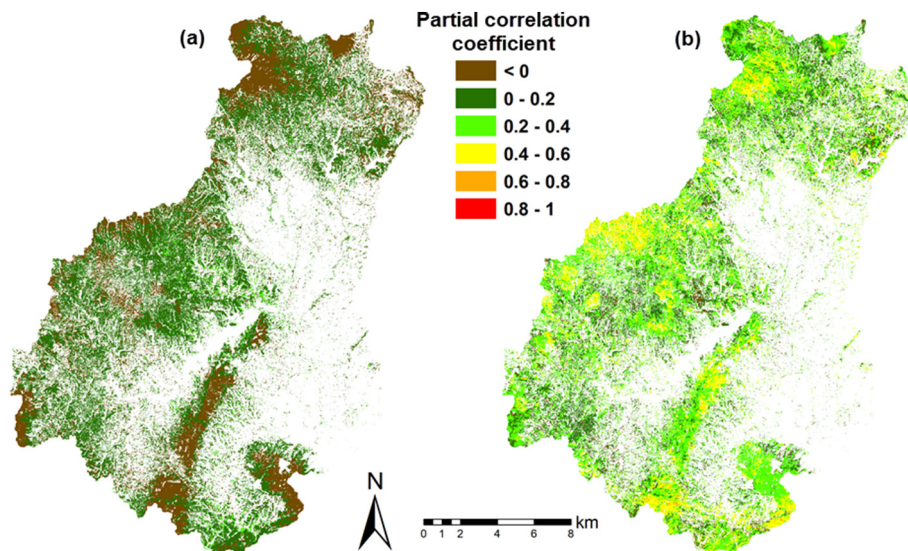


Fig. 16. Partial correlation coefficients among EVI and precipitation (a) and minimum temperature (b) on annual scale.

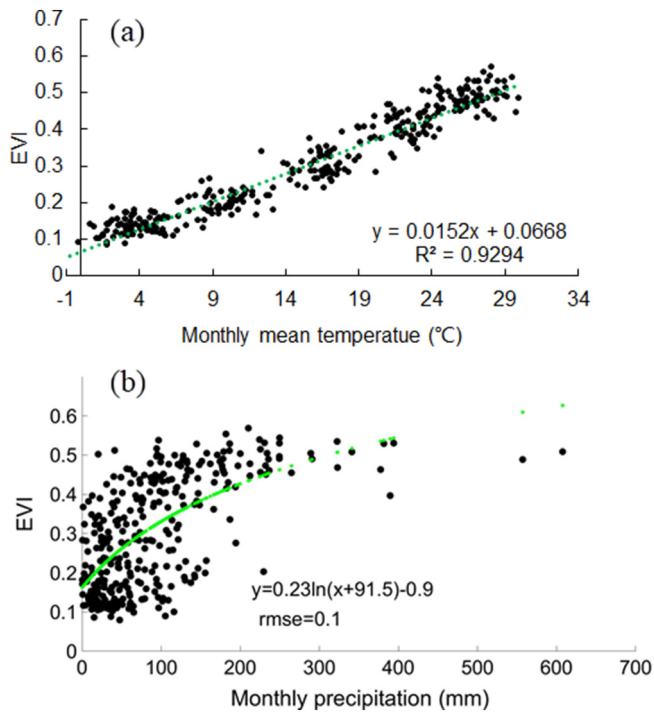


Fig. 17. Scatter graph of mean temperature (a), precipitation (b) and EVI.

#### 4.3.4. Quantitative relationship among EVI and climatic factors

As presented in Table 4, climate factors and EVI exhibit a good correlation on monthly scale, where temperature (especially for minimum temperature) and precipitation are two dominant control factors of EVI (referring to Section 4.3.2). Besides, due to the fact that both mean temperature and minimum temperature show high partial correlation with EVI and the data of mean temperature are often easier to collect, mean temperature, precipitation are thus finally selected to establish the quantitative relationship with EVI. On the other hand, the factor selection is also consistent with the fact that water and energy are two key factors for vegetation growth, where precipitation represents for water and temperature represents for energy.

To intuitively illustrate the relationships among EVI and climatic factors, Fig. 17 provides the scatter graph of EVI and precipitation, and mean temperature (Tmean) on monthly scale. It can be observed that EVI has high linear correlations with mean temperature and EVI keeps a stable level at about 0.45 after precipitation is over a threshold of about 200 mm/month.

Based on the monthly data and the above relations (Fig. 17), least square method is used to establish the quantitative relationship among EVI and climatic factors under different precipitation conditions, which can be written as follows (Eq. (3)). The root mean square errors are 0.0346 and 0.0277 for precipitation below and above 200 mm, respectively.

$$\text{EVI} = \begin{cases} 0.0143 \text{ Tmean} + 0.0091 \text{ Ln}(P) + 0.414, & P < 200 \text{ mm} \\ 0.0158 \text{ Tmean} + 0.0757, & P \geq 200 \text{ mm} \end{cases} \quad (3)$$

where EVI is enhanced vegetation index, Tmean represents the mean temperature, P means precipitation.

## 5. Conclusion

In this study, we assessed the forest cover change responding to climate in a subtropical humid monsoon area in China, using Landsat imagery with human-induced land cover change effect excluded. Taking the Qingliu River catchment as an example, the key findings are

summarized as follows. (1) Relative to forest cover in December 1988, 22.07% of the forest area has experienced land cover change including both deforestation and reforestation. (2) EVI shows a significant increasing ( $p < 0.01$ ) trend over the entire period (1989–2014), with increasing ( $p < 0.05$ ) during 2001–2014 before decreasing ( $p > 0.05$ ) during 1989–2000. (3) The spatial distribution of EVI is distinct in summer and growing season. (4) EVI and minimum temperature show higher correlation than those between EVI and precipitation, which is consistent with findings in other energy-limited areas. (5) Precipitation and pan evaporation showed accumulative lag effects (4 months) on forest EVI, while temperature has no lag effect. (6) Threshold of precipitation at 200 mm is identified. Quantitative relationship among EVI and climatic factors is established under different precipitation conditions.

Due to the exclusion of the effect of human-induced land cover change and the high resolution of the Landsat data, the proposed framework provides a more precise way to assess the climate impact on forest cover. The proposed framework is also applicable for assessing climate change impact on other vegetation types in other areas. The findings should provide scientific support for local forest management and ecosystem services, and also lay foundations for hydrologic effect assessment of forest cover change induced by climate change.

## Acknowledgment

This work has been financially supported by National Key Research and Development Program of China [grant numbers 2016YFA0601501, 2016YFB0502303]; National Natural Science Foundation of China [grant numbers 41601025, 61403062, 41830863, 41330854], State Key Laboratory of Hydrology-Water Resources and Hydraulic Engineering [grant number 2017490211], Science-Technology Foundation for Young Scientist of Sichuan Province [grant number 2016JQ0007], Sichuan Provincial Soft Science Research Program [grant number 2017ZR0208], and Fok Ying Tong Education Foundation for Young Teachers in the Higher Education Institutions of China [Grant number 161062].

## Appendix A. Supplementary data

Supplementary data to this article can be found online at <https://doi.org/10.1016/j.scitotenv.2018.12.290>.

## References

- Bartholomé, E., Belward, A.S., 2005. GLC2000: a new approach to global land cover mapping from Earth observation data. *Int. J. Remote Sens.* 26 (9), 1959–1977.
- Carlson, T.N., Ripley, D.A., 1997. On the relation between NDVI, fractional vegetation cover, and leaf area index. *Remote Sens. Environ.* 62 (3), 241–252.
- Donohue, R.J., McVICAR, T.R., Roderick, M.L., 2009. Climate-related trends in Australian vegetation cover as inferred from satellite observations, 1981–2006. *Glob. Chang. Biol.* 15 (4), 1025–1039.
- Epskamp, S., Fried, E.I., 2018. A tutorial on regularized partial correlation networks. *Psychol. Methods* 23 (4), 617–634.
- Fang, Q., Wang, G., Liu, T., Xue, B.L., Yinglan, A., 2018. Controls of carbon flux in a semi-arid grassland ecosystem experiencing wetland loss: vegetation patterns and environmental variables. *Agric. For. Meteorol.* 259, 196–210.
- Gao, Q., Guo, Y., Xu, H., Ganjurjav, H., Li, Y., Wan, Y., Liu, S., 2016. Climate change and its impacts on vegetation distribution and net primary productivity of the alpine ecosystem in the Qinghai-Tibetan Plateau. *Sci. Total Environ.* 554, 34–41.
- Giri, C., Pengra, B., Zhu, Z., Singh, A., Tieszen, L.L., 2007. Monitoring mangrove forest dynamics of the Sundarbans in Bangladesh and India using multi-temporal satellite data from 1973 to 2000. *Estuar. Coast. Shelf Sci.* 73 (1–2), 91–100.
- Hong, Y., Nix, H.A., Hutchinson, M.F., Booth, T.H., 2010. Spatial interpolation of monthly mean climate data for China. *Int. J. Climatol.* 25 (10), 1369–1379.
- Hou, W., Gao, J., Wu, S., Dai, E., 2015. Interannual variations in growing-season NDVI and its correlation with climate variables in the southwestern karst region of China. *Remote Sens.* 7 (9), 11105–11124.
- Huang, C., Goward, S.N., Masek, J.G., Thomas, N., Zhu, Z., Vogelmann, J.E., 2010. An automated approach for reconstructing recent forest disturbance history using dense Landsat time series stacks. *Remote Sens. Environ.* 114 (1), 183–198.
- Huete, A., Didan, K., Miura, T., Rodriguez, E.P., Gao, X., Ferreira, L.G., 2002. Overview of the radiometric and biophysical performance of the MODIS vegetation indices. *Remote Sens. Environ.* 83 (1–2), 195–213.

- Hutchinson, M.F., Xu, T., 2004. Anusplin Version 4.2 User Guide. Centre for Resource and Environmental Studies. The Australian National University, Canberra, p. 54.
- Jiang, L., Bao, A., Guo, H., Ndayisaba, F., 2017. Vegetation dynamics and responses to climate change and human activities in Central Asia. *Sci. Total Environ.* 599, 967–980.
- Jönsson, P., Cai, Z., Melaas, E., Friedl, M.A., Eklundh, L., 2018. A method for robust estimation of vegetation seasonality from Landsat and sentinel-2 time series data. *Remote Sens.* 10 (4), 635.
- Kendall, M.G., 1975. Rank Correlation Methods. Charles Griffin, London, p. 1975.
- Lamchin, M., Lee, W.K., Jeon, S.W., Wang, S.W., Lim, C.H., Song, C., Sung, M., 2017. Long-term trend and correlation between vegetation greenness and climate variables in Asia based on satellite data. *Sci. Total Environ.* 618, 1089–1095.
- LCMAP, 2018. Land Change Monitoring, Assessment, and Projection (LCMAP). <https://eros.usgs.gov/science/lcmmap>.
- Liu, J., Zhang, Z., Xu, X., Kuang, W., Zhou, W., Zhang, S., Jiang, N., 2010. Spatial patterns and driving forces of land use change in China during the early 21st century. *J. Geogr. Sci.* 20 (4), 483–494.
- Luo, Z., Yu, S., 2017. Spatiotemporal variability of land surface phenology in China from 2001–2014. *Remote Sens.* 9 (1), 65.
- Mann, H.B., 1945. Nonparametric tests against trend. *Econometrica: Journal of the Econometric Society* 245–259.
- Olofsson, P., Van Laake, P.E., Eklundh, L., 2007. Estimation of absorbed PAR across Scandinavia from satellite measurements: part I: incident PAR. *Remote Sens. Environ.* 110 (2), 252–261.
- Pinzon, J.E., Tucker, C.J., 2014. A non-stationary 1981–2012 AVHRR NDVI3g time series. *Remote Sens.* 6 (8), 6929–6960.
- Rehman, B., Liu, C., Wang, L., 2017. Least square method. *J. Electr. Eng. Technol.* 12 (1), 39–44.
- Restrepo, A.M.C., Yang, Y.R., Hamm, N.A., Gray, D.J., Barnes, T.S., Williams, G.M., ... Clements, A.C., 2017. Land cover change during a period of extensive landscape restoration in Ningxia Hui autonomous region, China. *Sci. Total Environ.* 598, 669–679.
- Rodriguez-Galiano, V.F., Ghimire, B., Rogan, J., Chica-Olmo, M., Rigol-Sanchez, J.P., 2012. An assessment of the effectiveness of a random forest classifier for land-cover classification. *ISPRS J. Photogramm. Remote Sens.* 67, 93–104.
- Shadmani, M., Marofi, S., Roknian, M., 2012. Trend analysis in reference evapotranspiration using Mann-Kendall and Spearman's Rho tests in arid regions of Iran. *Water Resour. Manag.* 26 (1), 211–224.
- Shen, Q., Gao, G., Han, F., Xiao, F., Ma, Y., Wang, S., Fu, B., 2018. Quantifying the effects of human activities and climate variability on vegetation cover change in a hyper-arid endorheic basin. *Land Degrad. Dev.* <https://doi.org/10.1002/ldr.3085>.
- Sun, W., Song, X., Mu, X., Gao, P., Wang, F., Zhao, G., 2015. Spatiotemporal vegetation cover variations associated with climate change and ecological restoration in the Loess Plateau. *Agric. For. Meteorol.* 209, 87–99.
- Sykes, Martin T., September 2009. Climate change impacts: Vegetation. *Encyclopedia of Life Sciences (ELS)*. John Wiley & Sons, Ltd., Chichester.
- Tan, X., Gan, T.Y., Chen, Y.D., 2018. Synoptic moisture pathways associated with mean and extreme precipitation over Canada for summer and fall. *Clim. Dyn.* 13, 1–21.
- Theurillat, J.P., Guisan, A., 2001. Potential impact of climate change on vegetation in the European Alps: a review. *Clim. Chang.* 50 (1–2), 77–109.
- Torres, S.d.S.A., Moisés, S.e.S.C., 2013. Seasonality, interannual variability, and linear tendency of wind speeds in the Northeast Brazil from 1986 to 2011. *Sci. World J.* 490857.
- Vitousek, P.M., Mooney, H.A., Lubchenco, J., Melillo, J.M., 1997. Human domination of Earth's ecosystems. *Science* 277 (5325), 494–499.
- Walther, G.R., Post, E., Convey, P., Menzel, A., Parmesan, C., Beebee, T.J., Bairlein, F., 2002. Ecological responses to recent climate change. *Nature* 416 (6879), 389.
- Wang, X., Piao, S., Ciais, P., Li, J., Friedlingstein, P., Koven, C., Chen, A., 2011. Spring temperature change and its implication in the change of vegetation growth in North America from 1982 to 2006. *Proc. Natl. Acad. Sci.* 108 (4), 1240–1245.
- Wen, Z., Lees, B.G., Feng, J., Lei, W., Shi, H., 2010. Stratified vegetation cover index: a new way to assess vegetation impact on soil erosion. *Catena* 83 (1), 87–93.
- Wen, Z., Wu, S., Chen, J., Lü, M., 2017. NDVI indicated long-term interannual changes in vegetation activities and their responses to climatic and anthropogenic factors in the Three Gorges Reservoir Region, China. *Sci. Total Environ.* 574, 947–959.
- Wu, D., Zhao, X., Liang, S., Zhou, T., Huang, K., Tang, B., Zhao, W., 2015. Time-lag effects of global vegetation responses to climate change. *Glob. Chang. Biol.* 21 (9), 3520–3531.
- Yang, Q., Scholz, M., Shao, J., Wang, G., Liu, X., 2017. A generic framework to analyse the spatiotemporal variations of water quality data on a catchment scale. *Environ. Model. Softw.* <https://doi.org/10.1016/j.envsoft.2017.11.003>.
- Yang, Q., Zhang, H., Wang, G., Luo, S., Chen, D., Peng, W., Shao, J., 2019. Dynamic runoff simulation in a changing environment: a data stream approach. *Environ. Model. Software* 112, 157–165.
- Yin, H., Pflugmacher, D., Li, A., Li, Z., Hostert, P., 2018. Land use and land cover change in Inner Mongolia-understanding the effects of China's re-vegetation programs. *Remote Sens. Environ.* 204, 918–930.
- Zhang, J., Pu, L., 2008. On coordination between urbanization and farmland area of Chuzhou City in recent 30 years. *Soil* 40 (4), 523–528 (In Mandarin).
- Zhang, Z., Chang, J., Xu, C.Y., Zhou, Y., Wu, Y., Chen, X., ... Duan, Z., 2018. The response of lake area and vegetation cover variations to climate change over the Qinghai-Tibetan Plateau during the past 30 years. *Sci. Total Environ.* 635, 443–451.
- Zhou, Y., Zhang, L., Fensholt, R., Wang, K., Vitkovskaya, I., Tian, F., 2015. Climate contributions to vegetation variations in central Asian drylands: pre-and post-USSR collapse. *Remote Sens.* 7 (3), 2449–2470.
- Zhu, Z., Fu, Y., Woodcock, C.E., Olofsson, P., Vogelmann, J.E., Holden, C., ... Yu, Y., 2016. Including land cover change in analysis of greenness trends using all available Landsat 5, 7, and 8 images: a case study from Guangzhou, China (2000–2014). *Remote Sens. Environ.* 185, 243–257.
- Zhu, Z., Wang, S., Woodcock, C.E., 2015. Improvement and expansion of the Fmask algorithm: cloud, cloud shadow, and snow detection for Landsats 4–7, 8, and Sentinel 2 images. *Remote Sens. Environ.* 159, 269–277.
- Zhu, Z., Woodcock, C.E., 2014. Continuous change detection and classification of land cover using all available Landsat data. *Remote Sens. Environ.* 144, 152–171.
- Zuo, D., Xu, Z., Yao, W., Jin, S., Xiao, P., Ran, D., 2016. Assessing the effects of changes in land use and climate on runoff and sediment yields from a watershed in the loess plateau of China. *Sci. Total Environ.* 544, 238–250.